

## Boron-10 conversion layer for ultra-cold neutron detection

---

**B. Clement<sup>1</sup> A. Bes<sup>1</sup> A. Lacoste<sup>1</sup> R. Combe<sup>3</sup> V. V. Nesvizhevsky<sup>2</sup> G. Pignol<sup>1</sup> D. Rebreyend<sup>1</sup> Y. Xi<sup>1</sup>**

<sup>1</sup>*LPSC, Université Grenoble Alpes, CNRS/IN2P3, Grenoble, France*

<sup>2</sup>*Institut Laue-Langevin, Grenoble, France*

<sup>3</sup>*Normandie Univ, ENSICAEN, UNICAEN, CNRS/IN2P3, LPC Caen, 14000 Caen, France*

*E-mail: [bclement@lpsc.in2p3.fr](mailto:bclement@lpsc.in2p3.fr)*

**ABSTRACT:** We report on the development of a  $^{10}\text{B}$  conversion layer optimized for ultra-cold neutron detection with silicon detectors. The efficiency of this layer is high and roughly uniform over a large ultra-cold neutron velocity range. The designed titanium-boron-nickel multilayer film was deposited on silicon using a microwave plasma-assisted co-sputtering method (first, for test purpose, on silicon wafers, then directly on the surface of a CCD sensor). The obtained sensor was then tested using both cold and ultra-cold neutrons.

**KEYWORDS:** ultracold neutrons, plasma PVD, boron-10

---

## Contents

<b>1</b>	<b>Introduction</b>	<b>1</b>
<b>2</b>	<b><sup>10</sup>B-based conversion layer design</b>	<b>2</b>
2.1	UCN interaction through thin layers	3
2.2	Titanium-Boron-Nickel multilayer	4
<b>3</b>	<b>Boron coating with plasma assisted PVD</b>	<b>5</b>
<b>4</b>	<b>Tests with neutrons</b>	<b>9</b>
<b>5</b>	<b>Conclusion</b>	<b>10</b>

---

## 1 Introduction

When neutrons are slowed down to kinetic energies below 100 neV, they are totally reflected by most surfaces at any incidence angle. These *ultra-cold neutrons* (UCN) constitute a sensitive tool to study fundamental interactions and symmetries [1]. In particular, ultra-cold neutrons are used to study gravity in a quantum context [2–5]. A neutron bouncing on top of an horizontal mirror realizes a quantum well problem and the vertical motion of the neutron bouncer has discrete energy states. The wave functions associated to the stationary quantum states have a spatial extension governed by the parameter  $z_0 = (\hbar^2/2m_n^2g)^{1/3} \approx 6 \mu\text{m}$ . Therefore, observing the spatial structure of the quantum states requires position-sensitive neutron detectors with a micrometric spatial resolution.

The first generation of gravitational neutron quantum states experiments employed CR39 solid-state nuclear-track detectors. These are polymer plates used to record the tracks of heavy charged ionizing particles. The tracks are revealed after a chemical etching process and then read out with an optical microscope. To be sensitive to neutrons, the plastic plate is coated with a thin conversion layer converting the neutrons into energetic charged particles. Only four stable nuclei can convert slow neutrons to charged particles: <sup>3</sup>He, <sup>6</sup>Li, <sup>10</sup>B and <sup>235</sup>U. Isotopically enriched <sup>235</sup>U was used in [6, 7] whereas [8] used <sup>10</sup>B. The plastic detectors achieve a good spatial resolution ( $\sigma \approx 2 \mu\text{m}$  RMS in both cases) but suffer from significant deformation during the etching process. Such deformation can be corrected for, however this a complex procedure and a source of systematic uncertainties. Neutron detectors based on fined-grained nuclear emulsion can provide much higher resolution [9]. However, they lack the real-time readout capability.

To overcome these severe limitations, semiconductor-based detectors have been recently investigated. In [10, 11], a silicon pixel device coated with <sup>6</sup>LiF was exposed to ultra-cold neutrons. With a matrix of  $256 \times 256$  square pixels with a pitch of  $55 \mu\text{m}$ , a spatial resolution of  $5 \mu\text{m}$  (FWHM) was measured. Sub-pixel resolution is achieved with the barycenter method of adjacent pixels. In [12], a commercial CMOS chip with an active area of  $3.2 \text{ mm} \times 4.8 \text{ mm}$  and a pitch of  $3 \mu\text{m}$  was

tested. The conversion layer was coated on a AlMg<sub>3</sub> foil positioned in front of the sensor surface. Two different neutron converters, <sup>10</sup>B and <sup>6</sup>LiF were compared. Although the spatial resolution of such a device was not measured, it could be estimated to be  $\sigma \approx 0.3 \mu\text{m}$ . Last, [13] used a commercial back-illuminated CCD sensor (512 × 512 pixels with a pitch of 24  $\mu\text{m}$ ) covered with a neutron converter by vacuum evaporation. As converter material <sup>10</sup>B and <sup>6</sup>Li were compared and <sup>10</sup>B was found to be more suitable. The spatial resolution was measured to be  $\sigma = 3 \mu\text{m}$  with a beam of cold neutrons.

This article presents the development of a <sup>10</sup>B-based layer to be used on position sensitive detectors to measure the wave functions of the bouncing neutrons in the GRANIT instrument [14] at Institut Laue Langevin. Neutrons are converted in both a lithium and an helium nuclei in boron through the reaction :



In 94% of cases the lithium is produced in an excited state and an extra 477 keV gamma ray is emitted. The energies of the lithium nucleus and the alpha particle are  $E_{Li} = 841 \text{ keV}$  and  $E_{\alpha} = 1471 \text{ keV}$ , respectively. In the remaining 6% of cases, no gamma ray is emitted and the particle energies are  $E_{Li} = 1014 \text{ keV}$  and  $E_{\alpha} = 1775 \text{ keV}$ .

The report will focus on the design, realisation and performance of the conversion layer. Spatial resolution will be discussed in a separate article later. We chose a CCD sensor with a rectangular (rather than squared) active area, more adapted to the needed sensitive area of 300 mm × 0.5 mm. The CCD used is a Hamamatsu S11071-1106N sensor, without an entrance window. The measurement presented here were done using a specific electronics designed to read 8 sensors in series [15]. To maximize the detection efficiency, without compromising on the spatial resolution, <sup>10</sup>B should be used as a conversion material. Producing a stable and well controlled thin boron coating on silicon constitutes a major technological challenge. All previous studies used an evaporation technique. We have developed a reproducible process using plasma assisted physical vapor deposition.

The article is organized as follows. Section 2 presents the optimization of the conversion layer thickness and the calculation of the theoretical efficiency. Section 3 describes the new plasma coating process. Finally, section 4 reports the first test of the prototype with both cold and ultra-cold neutrons at ILL.

## 2 <sup>10</sup>B-based conversion layer design

The design of the conversion layer takes into consideration several effects: the conversion layer must be sufficiently thick to absorb most of the neutrons but thin enough to let the secondary charged particles escape towards the silicon detector with sufficient energy. The layer should not reflect neutrons either and remain chemically stable. As boron tends to get oxidized quickly, an external protective layer of a passivating material such as titanium or aluminum must be considered. As the absorption cross-section goes as the inverse of the neutron velocity, the faster neutrons will tend to enter deeper into the boron layer and potentially escape undetected. One way to compensate for this effect is to add a thin UCN mirror between the boron layer and the silicon substrate. This layer could also improve bonding. The conversion layer will therefore consist of a multilayer of several materials on top of a silicon substrate.

## 2.1 UCN interaction through thin layers

Interaction of ultra cold neutrons with surfaces arise from their coherent scattering on nuclei. The surface of a material can be considered as a potential step. The interaction of a neutron with a thin layer is a simple one-dimensional well or barrier quantum problem. This potential, called optical Fermi potential, is a function of the scattering length  $a$  and atomic density  $\rho$ :

$$V = \frac{2\pi\hbar^2}{m_n}\rho a, \quad (2.1)$$

where  $m_n$  is the neutron mass and  $\hbar$  the reduced Planck constant. In addition, absorption can be described by an imaginary potential, which will translate in an exponentially decreasing amplitude. This imaginary potential is defined in a similar way from the absorption scattering length  $a_c$ :

$$W = -\frac{2\pi\hbar^2}{m_n}\rho a_c, \quad a_c = -\frac{\sigma k}{4\pi\hbar}, \quad (2.2)$$

where  $\sigma$  is the absorption cross-section and  $k$  the neutron momentum. Since the cross section varies as  $1/k$ , the product  $\sigma k$  and therefore the potential is independent of the neutron velocity. The total potential is then:

$$U = V - iW. \quad (2.3)$$

Let's consider a structure composed of  $n$  layers of material with thickness  $\delta_{i=1..n}$  on a silicon substrate. This multilayer has  $n + 1$  interfaces that constitute as many quantum steps. The longitudinal momentum of a neutron with energy  $E$  within the  $i$ -th layer is:

$$k_i^2 = \frac{2m_n}{\hbar^2}(E - V_i + iW_i), \quad (2.4)$$

and the wave function is of the form:

$$\psi_i(x) = a_i e^{ik_i x} + b_i e^{-ik_i x}. \quad (2.5)$$

Imposing continuity of the wave function and its derivative at each interface, one can compute the total reflection, transmission and absorption of the multilayer through the boundary matrix, assuming that the wave going out of the last interface has only a forward propagating part ( $b_{n+1}$ ):

$$\begin{pmatrix} t \\ 0 \end{pmatrix} = \prod_{i=n+1}^1 \frac{1}{K_i + L_i} \begin{pmatrix} K_i e^{-L_i G_i} & L_i e^{-K_i G_i} \\ L_i e^{K_i G_i} & K_i e^{L_i G_i} \end{pmatrix} \begin{pmatrix} 1 \\ r \end{pmatrix} = M \begin{pmatrix} 1 \\ r \end{pmatrix}, \quad (2.6)$$

with

$$K_i = k_i + k_{i-1}, \quad L_i = k_i - k_{i-1}, \quad G_i = \sum_{j<i} i\delta_j, \quad (2.7)$$

where  $k_0$  and  $k_{n+1}$  are the momenta in vacuum in front of the first layer and in the silicon substrate respectively and  $r = \frac{b_0}{a_0}$ ,  $t = \frac{a_{n+1}}{a_0}$ . The total reflection  $R$ , transmission  $T$  and absorption  $A$  of the multilayer are then:

$$\begin{cases} R = |r|^2 = \left| \frac{M_{21}}{M_{22}} \right|^2, \\ T = \left| \frac{k_0}{k_{n+1}} \right| \frac{1}{|M_{22}|} \text{ if } E - V_{n+1} > 0, \text{ 0 if not,} \\ A = 1 - R - T. \end{cases} \quad (2.8)$$

**Table 1.** Effective potential for materials used in this study

Material	V (neV)	W (neV)
Titanium	-50.1	0.025
Aluminum	54.0	0.001
Nickel	245.2	0.030
Silicon	54.1	<0.001
<sup>10</sup> B, 96 % enriched	2.5	36.3

Quantum reflection of neutrons on the entrance layer might be a major source of inefficiency of the detector. Reflection happens both on the real and imaginary parts of the potential. For a negative real potential  $U = V = -v$ ,  $v > 0$ , which is the case of titanium, reflection is:

$$R_{\text{real}} = \frac{2E + v - 2\sqrt{E^2 + Ev}}{2E + v + 2\sqrt{E^2 + Ev}}, \quad (2.9)$$

whereas for an imaginary potential  $U = -iw$ :

$$R_{\text{imag}} = \frac{E + \sqrt{E^2 + w^2} - 2\sqrt[4]{E^4 + E^2w^2} \cos\left(\frac{1}{2} \arctan \frac{w}{E}\right)}{E + \sqrt{E^2 + w^2} + 2\sqrt[4]{E^4 + E^2w^2} \cos\left(\frac{1}{2} \arctan \frac{w}{E}\right)}. \quad (2.10)$$

For a same potential absolute value, reflection on an imaginary potential is always larger than reflection on a negative real potential.

## 2.2 Titanium-Boron-Nickel multilayer

To satisfy the requirements of the conversion layer, the materials for the layers must be chosen carefully. We used the model described in the previous section to optimize the width of the components of a <sup>10</sup>B-based multilayer. The Fermi potentials used in this document are summarized in table 1.

<sup>10</sup>B has a real Fermi potential close to zero, but a large imaginary potential which is obviously a requirement for neutron conversion. Titanium was preferred to aluminum for the passivation layer as it has a large negative real potential but small absorption. In addition, an enhancement effect appears if one considers a thin enough layer of titanium over the boron conversion layer as shown in figure 2 (left). A 20 nm layer should be thick enough to ensure both protection against oxidation and a good transmission for UCNs.

The reflective layer between the boron and the silicon substrate needs to have a large Fermi potential and good mechanical properties. Nickel is an obvious choice as it is commonly used for neutron guides. The neutron losses due to transmission through nickel are shown in figure 2 (right) for various layer thicknesses. Here again, a 20 nm layer seems to be an acceptable choice. The potential step structure of the multilayer is given in figure 1.

The width of the boron layer was chosen as to maximize the detection efficiency taking into account both neutron absorption and the charged particle energy loss in the layer. Furthermore, the efficiency should remain large in a range of UCN velocities up to  $7 \text{ m}\cdot\text{s}^{-1}$  (the velocity cut-off for the

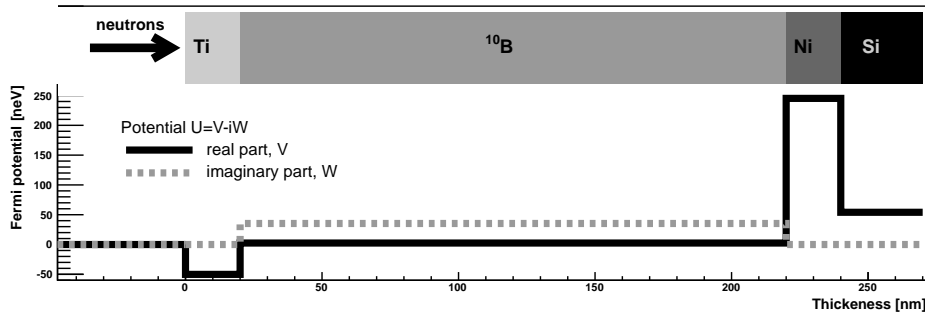


**Figure 1.** Structure of the Ti/ $^{10}\text{B}$ /Ni multilayer in term of real and imaginary potential.

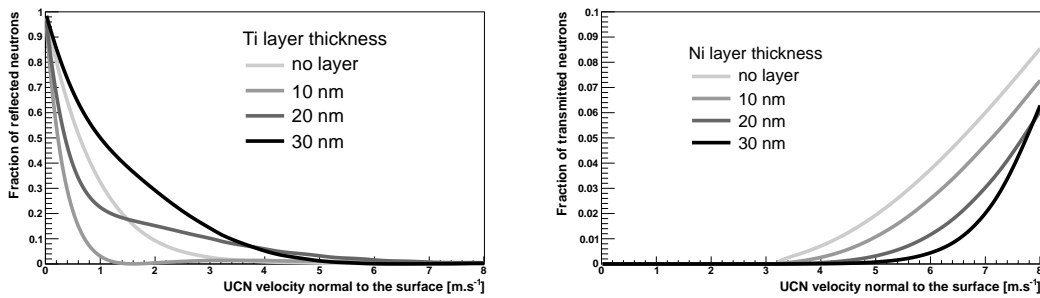


**Figure 2.** Reflection losses in a titanium-boron multilayer (left) and transmission losses through a boron-nickel multilayer on a silicon substrate as a function of the normal neutron velocity. The boron thickness is fixed to be 200 nm, titanium and nickel thickness vary from 0 to 30 nm (pale gray to black lines).

GRANIT UCN source). Monte-Carlo simulation using SRIM [16] as well as NIST databases [17] were used to estimate the energy loss. Charged particles with energies lower than 200 keV are assumed to be not detected in the silicon. The result of this optimisation is shown in figure 3 (left). For 200 nm, the efficiency is almost constant in the velocity range and start to decrease for thicker layers.

The expected detection efficiency for a 20 nm titanium, 200 nm enriched boron and 20 nm nickel multilayer on silicon, averaged over the velocity spectrum for the GRANIT UCN source is expected to be  $(86 \pm 1)\%$ . Finally, we show a summary of the effect of the titanium and nickel layers in figure 3 (right). The titanium layer reduces the efficiency for lower velocities but increases the uniformity of the efficiency. Protection from oxidization remains its main role, with acceptable efficiency loss. The nickel reflector is not crucial but helps to gain a few percent efficiency at higher velocities.

### 3 Boron coating with plasma assisted PVD

Thin films were deposited on room temperature substrate by microwave plasma-assisted co-sputtering method. The principal feature of this technology described in greater detail in [18, 19] is

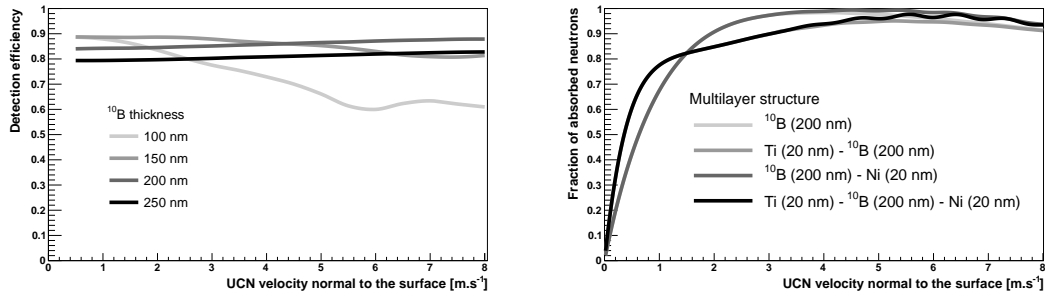


**Figure 3.** Left: total efficiency as a function of the neutron velocity for thicknesses of 100 nm, 150 nm and 200 nm of enriched boron. Efficiency includes neutron absorption probability and energy losses of secondary particles, for a detection energy threshold of 200 keV. Right: Neutron absorption of a boron multilayer as a function of the neutron normal velocity for a boron thickness of 200 nm showing the effect of the presence of a titanium entrance layer of a nickel reflector.

the separation of the plasma production (regulated by the microwave power) from the polarization of the surfaces involved in the deposition process. This separation allows, on the one hand, an independent and individual polarization of a set of targets making possible the individual control of their sputtering rate through the potential which is applied to each of them. On the other hand, the substrate can be either polarized or kept at ground potential according to the desired ion assistance during plasma processing. Moreover, the decoupling of the process parameters enables the implementation of in-situ sequential processes such as the substrate cleaning, targets cleaning and multilayer deposition without any exposure of samples outside the plasma reactor.

Multilayer films Ni/<sup>10</sup>B/Ti were directly deposited onto CCD sensors by successive sputtering of Ni, <sup>10</sup>B and Ti targets. For all process steps, an Ar plasma was sustained by 2 kW of microwave power through 24 wave couplers evenly distributed on the plasma chamber wall. Vacuum and working pressures were of 10<sup>-4</sup> Pa and 0.13 Pa, respectively. The multi-targets holder (see figure 4) is placed on top of the chamber at an adjustable distance away from the substrate on which the films are ultimately grown. After a prior cleaning process of 10 min in an ethanol sonic bath, the substrate is submitted during 20 min in Ar plasma to an ion bombardment with an energy around 50 eV. This results from 30 V of DC self-bias (by applying 50 W of RF power) added to 20 V of plasma potential.

During the deposition process, one Ni target, three <sup>10</sup>B and three Ti targets, with a 99.99% purity for each of them, are positioned on the target holder in the configuration shown in figure 4. They were consecutively biased at different voltages and for different times: -100 V (DC bias) during 23 min for Ni target, -440 V (RF bias) during 240 min for <sup>10</sup>B and -100 V (DC bias)/18 min for Ti. For a distance between the targets and substrate fixed at 150 mm, the above process parameters were determined by a prior calibration operation (performed on silicon substrate) for obtaining the following coating on each sensor: 20 nm, 200 nm and 20 nm of Ni, <sup>10</sup>B and Ti, respectively. The deposition was initiated once the target cleaning has been carried out by simultaneously applying -600 V of DC bias to the metal targets (Ni and Ti) and 440 V of DC self-bias (250 W of RF power) to the boron dielectric target.



**Figure 4.** Targets holder for multilayer film (Ni/<sup>10</sup>B/Ti) deposition.

For direct deposition on sensors, a special copper holder was designed to guarantee the thermal transfer and the electrical contact between the sensor and the holder during deposition, the latter being electrically kept grounded and thermally at the room temperature by water cooling. The thermal transfer was optimized using graphite based interface pad (Tgon™ 820, from Laird Technologies) on the lateral sides. The CCD holder was then placed on the substrate holder and fastened in place with silver lacquer and screws.

The microstructure of deposited films on Si substrates and also their thickness were examined by SEM (scanning electron microscope) using Zeiss Ultra+ Field Emission SEM (EHT voltage levels of 3 kV). The preliminary calibration step clearly pointed out the consequence of the surface plasma cleaning, especially that of the substrate. Indeed, this leads not only to the removing of hydrocarbon impurities and/or native oxides but also to the creation of a slight surface roughness. In this way, the adhesion to the substrate of the growing film is greatly improved and the impact of the compressive stress strongly diminished. Figure 5 compares a boron film deposited on a plasma cleaned silicon substrate for 10 min to the one obtained with a plasma cleaning for 20 min (argon plasma at a pressure of 0.13 Pa and 50 W of RF power applied to the substrate). For a not enough bias voltage or processing time, the grown film exhibits a compressive stress leading to the delamination in form of flakes (figure 5, left side). An appropriate plasma cleaning allows growing of a compact film with a good adhesion to the substrate surface (figure 5, right side). The same compact microstructure can be observed in figure 6 for a multilayer film (with a boron thickness of 300 nm) deposited on a silicon substrate. A good adhesion to the substrate and well delimited interfaces between the three layers can be observed.

The use of multilayer structured coatings for the stress reduction without post-deposition annealing was already reported in [20] for boron-carbon multilayer coating by RF plasma sputtering. However, the multilayer with a thickness of about 330 nm includes six layers of the same B-C coating obtained in the sequential manner. The method used in this work enables to obtain the neutron

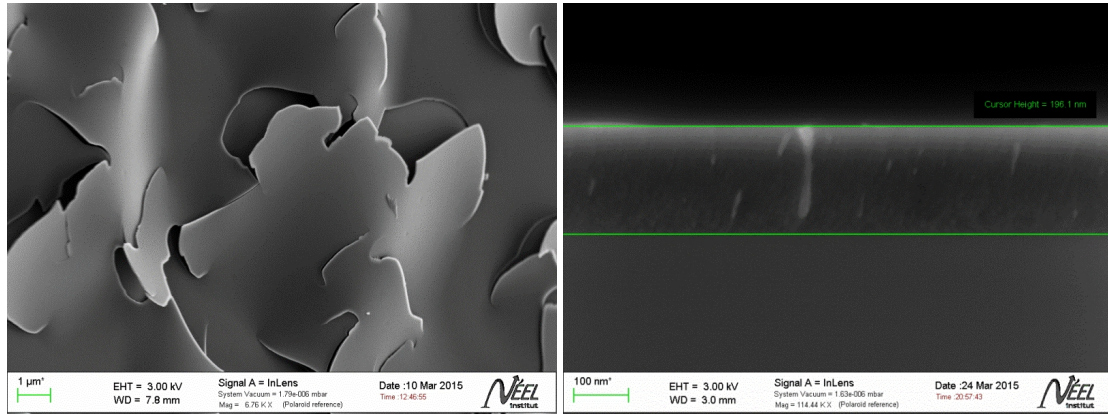


**Figure 5.** A boron film deposited on a plasma cleaned silicon substrate with 50 W of RF polarization, for a six hours deposition process: on the left for 10 minutes cleaning (top view) and on the right for 20 minutes (cross section view). In this last case, the thickness of the layer is 196 nm.

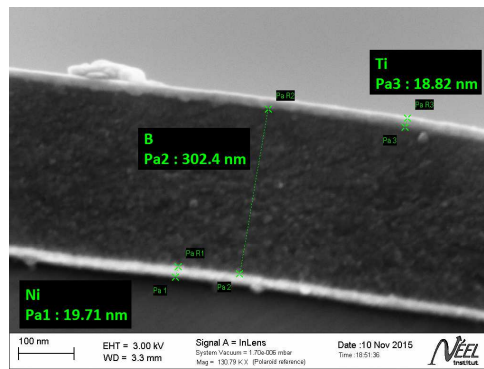


**Figure 6.** A cross section of a multilayer Ti/B/Ni (20 / 300 / 20 nm) film grown onto a silicon substrate. Each layer is measured at a random point and the thickness are found to be 18.8 nm (Ti), 302.4 nm (B) and 19.7 nm (Ni) with a precision of 1 nm.

reactive layer (of 200 nm on sensor, with a deposition rate of about  $0.75 \text{ nm}\cdot\text{min}^{-1}$ ) in a single sequence while the two other sequences are used for deposition on both sides of the boron film of two additional layers of different natures: Ni and Ti. The first promotes not only a increased adherence but also the reflection back into the reactive layer of the unconverted UCNs during their first crossing. The second protects the boron layer against oxidization thereby ensuring its chemical stability.

An example of CCD sensor coated is given in figure 7. The functional properties of the multilayer coatings on the sensor and aging behavior were only evaluated through the CCD sensor performance as described in section 4 .

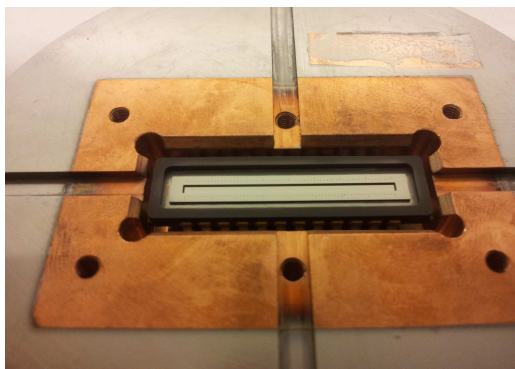


**Figure 7.** A coated CCD sensor inside of the copper holder.

#### 4 Tests with neutrons

The range in silicon of the ions produced in the neutron absorption on boron does not exceed a few microns with an even smaller lateral straggling. As we used a pixelized detector, the produced charge will drift within the bulk silicon and several pixels are hit. The position could therefore be reconstructed using a weighted average over a cluster of pixels. The central pixel contains between a fourth and a fifth of the total energy and 99% is contained in a 9 by 9 pixels matrix around the center, for both lithium and helium ions. On this basis, we constructed a simple clustering algorithm. For each image, a  $3 \times 3$  sliding window is applied to determine seed clusters whose total ADC count exceed a given threshold. Each cluster is afterwards characterized by three variables: the reconstructed horizontal and vertical positions and the sum of ADC counts in the cluster which represent the total charge in arbitrary units. A 30 kBq  $^{241}\text{Am}$   $\alpha$  source attenuated through 30 to 40 mm of air was used to calibrate the energy response. Data from NIST databases are used to estimate the alpha particle energy loss. Energy measurement in itself is not the aim for the detector, but it can be used to ensure that the observed signal comes from the neutron absorption on boron.

Two coated sensors were tested with neutrons at ILL several months after the deposition of the conversion layer. The first test consisted of exposing the sensors to a cold neutron beam at the PF1b beam line [21]. This beam line produces a neutron beam with a mean wavelength of 4 to 4.5 Å with a flux of  $1.8 \times 10^{10}$  n.cm<sup>-2</sup>.s<sup>-1</sup> Neutrons were collimated through a 50 μm slit made by two 10 cm long glass plates with rough surfaces to avoid the specular reflection of neutrons. The surface of the sensor was placed a few millimeters downstream the output of the slit. The slit image obtained on both sensors can be seen in figure 8. The first sensor had a completely adhering boron layer, whereas the other presented cracks and flakes. As a result a clear loss of spatial resolution and efficiency can be qualitatively observed on the second sensor. This measurement allows for a high flux, but is not useful to measure the efficiency as the layer is optimized for ultra cold neutrons.

The coated sensor was also exposed to ultra-cold neutrons using the SUN source of the GRANIT facility at ILL. The energy deposited in the silicon detector is shown in figure 9. It shows the expected alpha and lithium peaks, as well as the more energetic alpha representing 6% of the absorptions. The left tail of the peaks comes from the varying length of boron traversed by the particle depending on the emission angle. A comparison to a SRIM simulation shows a good

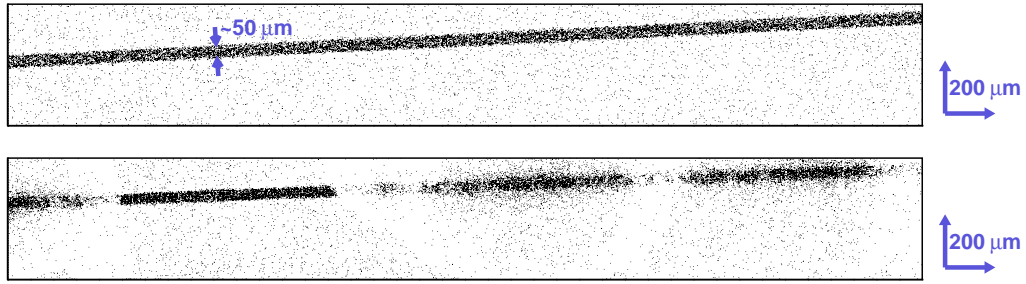


**Figure 8.** Impact position of the reconstructed alpha and lithium ions from cold neutrons out of a slit. On the top picture, the increased neutron flux at the slit level is clearly seen. On the bottom picture, fuzzy structures appear revealing a non adhering boron layer (flakes), which was confirmed visually.

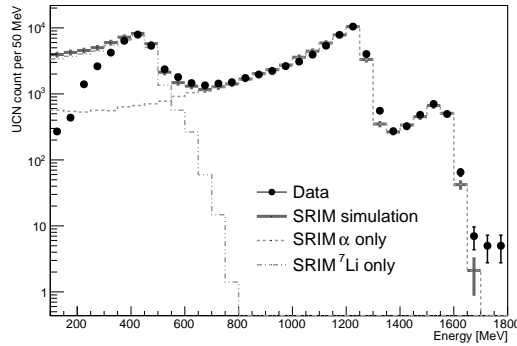


**Figure 9.** An energy spectrum of the detected charged particles together with a comparison to SRIM simulations for both alpha and lithium ions.

agreement.

The UCN flux was determined using a standard gaseous  $^3\text{He}$  UCN detector. The detector window is a  $15\ \mu\text{m}$  titanium foil, which accounts for  $24 \pm 1\%$  neutron loss either due to absorption or quantum reflection. This efficiency is estimated using Monte-Carlo simulation and the error is dominated by geometrical effects. The UCN flux on the sensor surface is therefore estimated as  $14 \pm 1.5\ \text{UCN}\cdot\text{cm}^{-2}\cdot\text{s}^{-1}$ . The flux measured by the sensor itself is  $11.41 \pm 0.12\ \text{UCN}\cdot\text{cm}^{-2}\cdot\text{s}^{-1}$ . The resulting efficiency is  $82 \pm 9\%$  which is consistent with the expectation discussed in section 2.

## 5 Conclusion

We studied ultra-cold neutron detectors based on a  $^{10}\text{B}$  conversion layer coupled to a silicon detector. Such a conversion layer needs several optimizations: thickness of the boron layer including both the conversion efficiency and the charged particles energy loss in the layer, effect of the passivation layer, reflective gain from the nickel layer. We showed that a multilayer composed of a 20 nm titanium protection layer on top a 200 nm enriched boron-10 and 20 nm nickel should provide a total conversion efficiency from 83% to 89% over a large range of neutron velocities. To this

end, a reliable process for boron deposition based on cold plasma sputtering has been developed. The multi target configuration of the plasma reactor allows for the production of the multilayer in one single process. Such a multilayer was produced on the surface of a CCD sensor. Neutrons measurement were performed at PF1b and GRANIT instrument at ILL providing respectively cold and ultracold neutrons to test the performances of the sensor. The total efficiency is found to be  $82 \pm 9\%$  which is in agreement with our expectations. We also showed that neutrons can be used to check the uniformity and adherence of the layer on a position sensitive detector. Nevertheless, the use of this sensor as a position sensitive detector will now require more detailed study of its spatial resolution.

## References

- [1] D. Dubbers and M. G. Schmidt, *The neutron and its role in cosmology and particle physics*, *Rev. Mod. Phys.* **83** (2011) 1111.
- [2] V. V. Nesvizhevsky et al., *Quantum states of neutrons in the earth's gravitational field*, *Nature* **415** (2002) 297.
- [3] V. V. Nesvizhevsky, *Near-surface quantum states of neutrons in the gravitational and centrifugal potentials*, *Physics Uspekhi* **53** (2010) 645.
- [4] T. Jenke et al., *Realization of a gravity-resonance-spectroscopy technique*, *Nature Phys.* **7** (2011) 468.
- [5] G. Pignol, *Probing dark energy models with neutrons*, *Int. J. Mod. Phys.* **A24** (2015) 1530048.
- [6] V. V. Nesvizhevsky et al., *Search for quantum states of the neutron in a gravitational field: gravitational levels*, *Nucl. Instrum. Methods* **A440** (2000) 754.
- [7] S. Baessler et al., *New methodical developments for GRANIT*, *Comptes Rendus Physique* **12** (2011) 729.
- [8] T. Jenke et al., *Ultracold neutron detectors based on  $^{10}\text{B}$  converters used in the qBounce experiments*, *Nucl. Instrum. Methods* **A732** (2013) 1.
- [9] N. Naganawa et al., *Ultracold neutron detectors based on  $^{10}\text{B}$  converters used in the qBounce experiments*, *Eur. Phys J.* **C78** (2018) 959.
- [10] J. Jakubek et al., *A coated pixel device timepix with micron spatial resolution for UCN detection*, *Nucl. Instrum. Methods* **A600** (2009) 651.
- [11] J. Jakubek et al., *Position-sensitive spectroscopy of ultra-coldneutron swith Timepix pixel detector*, *Nucl. Instrum. Methods* **A607** (2009) 45.
- [12] T. Lauer et al., *Experimental investigation of a low-cost solid state detector with high spatial resolution for ultracold neutrons*, *Eur. Phys. J.* **A47** (2011) 150.
- [13] S. Kawasaki et al., *Development of a pixel detector for ultra-cold neutrons*, *Nucl. Instrum. Methods* **A615** (2010) 42.
- [14] D. Roulier et al., *Status of the GRANIT facility*, *Adv. High Energy Phys.* **2015** (2015) 730437.
- [15] O. Bourrion et al., *C2D8: An eight channel CCD readout electronics dedicated to low energy neutron detection*, *Nucl. Instrum. Methods* **A880** (2018) 28.
- [16] J. P. B. J. F. Ziegler, M. D. Ziegler, *SRIM – The stopping and range of ions in matter*, *Nucl. Instrum. Methods* **B268** (2010) 1818.

- [17] M. Berger et al., *Stopping-power and range tables for electrons, protons, and helium ions*, NIST Standard Reference Database 124, National Institute of Standards and Technology, Gaithersburg, MD., [online] <https://dx.doi.org/10.18434/T4NC7P> (2018) .
- [18] H. Le-Quoc et al., *Thin films of thermoelectric compound Mg<sub>2</sub>Sn deposited by co-sputtering assisted by multi-dipolar microwave plasma*, *J. Alloys Compd.* **509** (2011) 9906.
- [19] H. Le-Quoc et al., *Deposition of thin films of Mg<sub>2</sub>Si<sub>1-x</sub>Sn<sub>x</sub> solid solution by plasma-assisted co-sputtering*, *J. Alloys Compd.* **538** (2012) 73.
- [20] E. Vassallo et al., *Deposition of boron–carbon multilayer coatings by RF plasma sputtering*, *Surf. Coat. Technol.* **214** (2013) 59.
- [21] H. Abele et al., *Characterization of a ballistic supermirror neutron guide*, *Nucl. Instrum. Meth.* **A562** (2006) 407.